JPE 16-5-18

http://dx.doi.org/10.6113/JPE.2016.16.5.1791
ISSN(Print): 1598-2092 / ISSN(Online): 2093-4718

# Consideration of the Carrier Based Signal Injection Method in Three Shunt Sensing Inverters for Sensorless Motor Control

Sungho Jung* and Jung-Ik Ha†

*,†School of Electrical and Computer Engineering, Seoul National University, Seoul, Korea

**Abstract**

This paper considers a carrier based signal injection method for use in the three shunt sensing inverter (TSSI) for sensorless motor control. It also analyzes the loss according to the injection axis of the voltage signal. To remove both the phase current and rotor position sensors, a sensorless method and a phase current reconstruction method can be simultaneously considered. However, an interaction between the two methods can be incurred when both methods inject voltage signals simultaneously. In this paper, a signal injection based sensorless method with the 120° OFF Discontinuous PWM (DPWM) is implemented in a TSSI to avoid this interaction problem. Since one leg does not have a switching event for one sampling period in the 120º OFF DPWM, the switching loss is altered according to the injection axis. The switching loss in the *d*-axis injection case can be up to 32% larger than that in the *q*-axis injection case. Other losses according to the injection axis are also analyzed.

**Key words:** AC motor, Phase current reconstruction, Sensorless control, Signal injection, Three shunt sensing inverter

## I. INTRODUCTION

Recently, inverter driven AC machines have become widely used in many industry home appliances such as refrigerators, air conditioners, and wash machines [1]. For a speed or torque control of an AC machine, the inverter modulates the phase voltage whose frequency and magnitude can be adjusted and this is applied to the AC machine. Here, the phase current and rotor position information are necessary for a high dynamic and efficient operation. A current transducer and a hall-effect sensor are commonly used in home appliances as the phase current and rotor position sensors, respectively. However, since these sensors are expensive, phase current reconstruction methods and sensorless controls have been studied to eliminate them.

In order to replace the current transducer, phase current reconstruction methods with a shunt resistor have been studied in many papers [2]-[7]. The phase current reconstruction method can be implemented in a single shunt sensing inverter (SSSI) and in a three shunt sensing inverter (TSSI). In the SSSI, one shunt resistor is installed between the DC link capacitor and the six bridges of the inverter [4]. In the TSSI, three shunt resistors are installed to the bottom of the lower switches [7]. Since the value of the shunt resistor is known, the current magnitude can be calculated by measuring the voltage of the shunt resistor. By mapping the current magnitude with the switch states, the phase current can be reconstructed. Here, the switching state is kept for a certain minimum amount of time to reconstruct the current signal clearly. This minimum amount of time incurs an immeasurable area in the space vector, and the operation area of the inverter is limited. To reduce this immeasurable area, the minimum voltage injection method in the SSSI [4] and the 120º OFF Discontinuous PWM (DPWM) instead of the continuous PWM in the TSSI can be considered [7].

In order to replace position sensors such as a hall-effect sensor, sensorless methods have been studied in many papers [8]-[17]. The sensorless methods are classified as back-EMF voltage based methods and signal injection based methods. In the former methods, the rotor angle is calculated from the estimated back-EMF voltages without any voltage signal injection or circuit modification [8]-[12]. The estimated rotor angle is accurate in the high speed range but not in the low

Manuscript received Apr. 18, 2016; accepted Jun. 5, 2016
Recommended for publication by Associate Editor Kwang-Woon Lee.
†Corresponding Author: jungikha@snu.ac.kr
Tel: +82-880-1760, Fax: +82-878-1452, Seoul Nat'l University
*Dept. of Electrical and Computer Eng., Seoul Nat'l University, Korea

speed range because of inverter nonlinearity. To overcome this drawback, the latter methods have been proposed [12]-[17]. From the rotor saliency caused by its shape or saturation effect, the current response by the injection voltage varies with the rotor angle. From this current response, the rotor angle can even be estimated at zero speed. Here, a high frequency signal is preferred for easy signal separation and rapid angle estimation [14], [15]. However, the injected voltage signal increases an audible noise and system losses.

However, when the phase current reconstruction and sensorless methods inject voltage signals simultaneously, a signal interaction can be incurred and the estimated rotor angle can have errors. In this paper, the signal injection based sensorless method and phase current reconstruction in the TSSI are considered to avoid this interaction problem. Here, the 120º OFF DPWM is implemented as the phase current reconstruction method to reduce the immeasurable area. In addition, the injection frequency in the signal injection based sensorless method is maximized at the carrier frequency to reduce the audible noise. Even though the machine loss according to the injection axis has been studied in [18], [19], there are not many studies on the inverter loss in the signal injection based sensorless method. Therefore, in this paper, the switching loss according to the injection axis is analyzed in detail. Firstly, the modified voltage vectors by the *d*-axis and *q*-axis voltage injections are compared in a vector diagram. From the switching loss equation, how the operating points change in each case are studies. These loss analyses are verified with simulation and experimental results.

A switching loss analysis of the carrier signal injection method in the TSSI has been introduced in [20]. In this paper, the possibility of the interaction problem between the phase current reconstruction methods and the sensorless methods are considered. In addition, more detailed loss analysis and experimental results are added based on [20].

This paper is organized as fallowed. In section II, the interaction problem between the phase current reconstruction methods and two types of sensorless methods are analyzed. In section III, the signal injection method in the TSSI is introduced. In section IV, the switching loss and other losses according to the injection axis are analyzed. Simulation and experimental results are shown in section V, and a conclusion is presented in section VI.

## II. Interaction Between Phase Current Reconstruction and Sensorless Methods

The possibility of an interaction problem between the phase current reconstruction methods and the sensorless methods are listed in Table I. When the two methods are considered together, there is no interaction problem if one or neither method uses an additional voltage signal. However, it can be incurred if both methods use an additional voltage signal.

In the minimum voltage injection method of the phase current reconstruction algorithm in the SSSI [4], the voltage vector is modified so that the reference voltage vector is in the immeasurable area. Here, the frequency of the injected voltage signal for the vector modification is the carrier frequency at zero speed. However, since additional voltage is not injected when the voltage vector is in the measurable range, the average frequency is changed to a non-zero speed. In the signal injection based sensorless control, a voltage signal from a few hundred Hertz to kilo-Hertz are normally injected. Therefore, the voltage signals for the phase current reconstruction and the sensorless method cannot be separated clearly when the frequencies of the two voltage signal are close. This can incur an error in the rotor angle estimation because of the interaction between the two voltage signals. In [21], the *d*-axis current is added to move the reference voltage vector to the measurable area [21]. However, this additional *d*-axis current increases the total system loss and the cause of the error in the rotor angle estimation is not completely eliminated. In [22], phase shift PWM can be considered in the SSSI. Regardless of the voltage vector for machine control, the 120° shifted carrier generates a rotating signal at the carrier frequency. However, this method cannot adjust the level of the rotating voltage signal and it needs many points of current samplings.

TABLE I
Interaction Problem between Phase Current Reconstruction and Sensorless Methods

| | | Phase Current Reconstruction | |
|---|---|---|---|
| | | Voltage inject. in SSSI | 120° OFF DPWM in TSSI |
| Sensorless Method | Signal inject. | *interaction* | *no problem* |
| | back-EMF | *no problem* | *no problem* |

Therefore, this paper considers a signal injection based sensorless method with the 120° OFF DPWM in the TSSI. Since the 120° OFF DPWM in the TSSI does not use any voltage signal injection, there is no interaction problem when the signal injection or the back-EMF based sensorless method is considered.

## III. Signal Injection Based Sensorless Method in the Three Shunt Sensing Inverter

### A. Pulsating Voltage Injection

Fig. 1 shows a block diagram of the signal injection based sensorless method. The command of the injection voltage is added to the output command of the current controller. The PWM inverter modulates the pole voltage which represents the mixed two commands. The current response by the modulated pole voltage consists of two frequency components. One is the rotating frequency component for the motor drive, and the other is the injection frequency component for the angle estimation. The former component is used as the feedback signal of the current controller after filtering the latter

component. The latter frequency component is extracted with signal processing and it is used to estimate the rotor angle and speeds.

The equation between the injection voltage and its current response is followed. In the low speed range, the back-EMF voltage is small and negligible. Therefore, the voltage equation at a high frequency in the rotor reference frame of a PMSM can be simplified as:

$$\begin{bmatrix} v_{dsh}^r \\ v_{qsh}^r \end{bmatrix} = \begin{bmatrix} L_d & 0 \\ 0 & L_q \end{bmatrix} \frac{d}{dt} \begin{bmatrix} i_{dsh}^r \\ i_{qsh}^r \end{bmatrix}, \quad (1)$$

where $L_d$ and $L_q$ are the $d$-axis and $q$-axis inductances, and $[\, v_{dsh}^r \,,\, v_{qsh}^r \,]^T$ and $[\, i_{dsh}^r \,,\, i_{qsh}^r \,]^T$ are the high frequency components of the $d$-axis and $q$-axis voltage and current in the real rotor reference frame, respectively. The current responses in the estimated rotor reference frame by the injection voltage are derived as:

$$\frac{d}{dt} \begin{bmatrix} i_{dsh}^{\hat{r}} \\ i_{qsh}^{\hat{r}} \end{bmatrix} = \frac{1}{L_d L_q} \begin{bmatrix} \Sigma L - \Delta L \cos 2\tilde{\theta}_r & -\Delta L \sin 2\tilde{\theta}_r \\ -\Delta L \sin 2\tilde{\theta}_r & \Sigma L + \Delta L \cos 2\tilde{\theta}_r \end{bmatrix} \begin{bmatrix} v_{dsh}^{\hat{r}} \\ v_{qsh}^{\hat{r}} \end{bmatrix}, \quad (2)$$

where $\tilde{\theta}_r$ is the angle error between the estimated and the real rotor angles, $\Sigma L$ is $(L_d + L_q)/2$, $\Delta L$ is $(L_d - L_q)/2$, and the superscript ' $\hat{r}$ ' means the estimated rotor reference frame.

When the square wave voltage with a magnitude of $V_{inj}$ is injected in the $d$-axis of the estimated rotor reference frame, the $d$-axis and $q$- axis current variations for half of the injection period ($\Delta T$) are:

$$\begin{bmatrix} \Delta i_{dsh}^{\hat{r}} \\ \Delta i_{qsh}^{\hat{r}} \end{bmatrix} = \frac{\Delta T \cdot V_{inj}}{L_d L_q} \begin{bmatrix} \Sigma L - \Delta L \cos 2\tilde{\theta}_r \\ -\Delta L \sin 2\tilde{\theta}_r \end{bmatrix}. \quad (3)$$

If the angle error is small, $\sin 2\tilde{\theta}_r$ can be approximated by $2\tilde{\theta}_r$. Therefore, the magnitude of the $q$-axis current variation is proportional to $\tilde{\theta}_r$. This magnitude of the $q$-axis current variation is used to estimate the rotor angle and speed with a PI type state filter or a Luenberger observer. When a square wave voltage is injected into the $q$-axis of the estimated rotor reference frame, the current variation by the positive injection voltage is:

$$\begin{bmatrix} \Delta i_{dsh}^{\hat{r}} \\ \Delta i_{qsh}^{\hat{r}} \end{bmatrix} = \frac{\Delta T \cdot V_{inj}}{L_d L_q} \begin{bmatrix} -\Delta L \sin 2\tilde{\theta}_r \\ \Sigma L + \Delta L \cos 2\tilde{\theta}_r \end{bmatrix}. \quad (4)$$

Here, the magnitude of the $d$-axis current variation is proportional to $\tilde{\theta}_r$ and it is used to estimate the rotor angle and speed. In the $d$-axis or $q$-axis injection, since the inductance values are used as the gain of the current ripple signal, an error in the inductance values do not incur a steady state error. If a voltage signal which includes both $d$-axis and $q$-axis components is injected into the estimated rotor reference frame, the exact inductance values of the machine are necessary to calculate $\tilde{\theta}_r$. Therefore, the error in the inductance values incurs a steady state error in the angle estimation. Therefore, the voltage signal is normally injected at the $d$-axis or the $q$-axis.

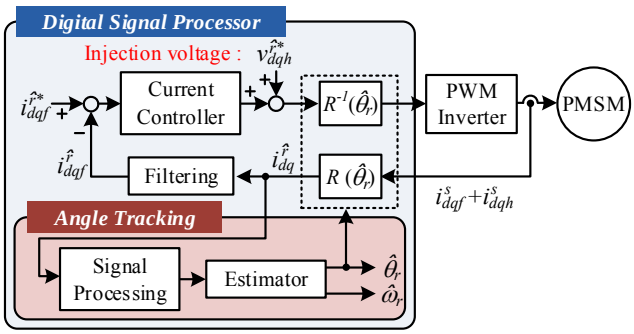


Fig. 1. Block diagram of the signal injection based sensorless method.

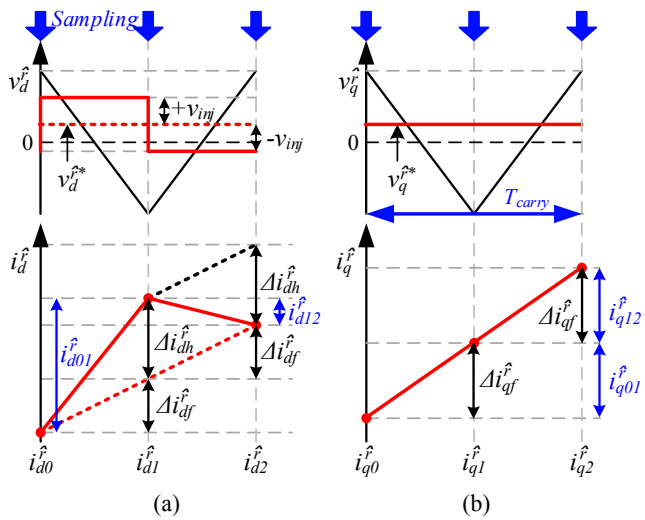


Fig. 2. Voltage references and current variations in the estimated rotor reference frame when the carrier frequency of the voltage signal is injected at $d$-axis. (a) $d$-axis voltage reference and current (b) $q$-axis voltage reference and current.

By calculating the difference between two sampled current signals, the magnitude of the $d$-axis or $q$-axis current variation can be calculated. In [15], a signal processing method where the carrier frequency signal is injected has been studied. The voltage references and the current variations are shown in Fig. 2. When the $d$-axis and $q$-axis voltage references for the current control ($v_{ds}^r$, $v_{qs}^r$) are constantly kept for one carrier period, a square wave voltage at the carrier frequency is added in the $d$-axis. Here, the current variation consists of two components. One is a current variation by the voltage reference for the current control ($\Delta i_{dqf}^{\hat{r}}$) and the other is a current variation by the injection voltage ($\Delta i_{dqh}^{\hat{r}}$). By sampling the current signals at the peak and valley of the carrier signal, the current variations between the sampling points can be calculated as:

$$\begin{aligned} i_{dq10}^{\hat{r}} &= i_{dq1}^{\hat{r}} - i_{dq0}^{\hat{r}} = \Delta i_{dqf}^{\hat{r}} + \Delta i_{dqh}^{\hat{r}} \\ i_{dq21}^{\hat{r}} &= i_{dq2}^{\hat{r}} - i_{dq1}^{\hat{r}} = \Delta i_{dqf}^{\hat{r}} - \Delta i_{dqh}^{\hat{r}} \end{aligned}. \quad (5)$$

From (5), the current variation by the injection voltage can be extracted as:

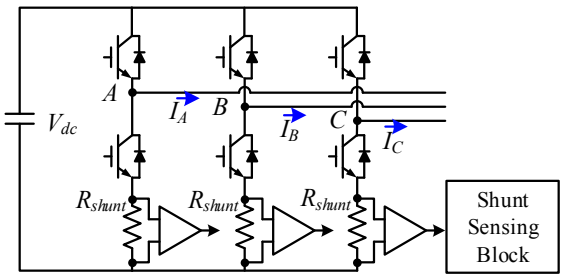


Fig. 3. Typical circuit of the three shunt sensing inverter.

$$\Delta i_{dqh}^{\hat{r}} = (i_{dq10}^{\hat{r}} - i_{dq21}^{\hat{r}})/2. \quad (6)$$

Therefore, the injection frequency component can be extracted from the current variation without a digital filter.

### *B. Current Sampling in the TSSI*

In the TSSI, three resistors are installed on the bottom of the lower switches, as shown in Fig. 3. When the lower switch is turned on ($S_x$=0, when $S_x$ is the switching function of the leg, and $x$ is a leg named $A$, $B$, or $C$), the phase current passes through the shunt resistor and its magnitude can be calculated. However, when the upper switch is turned on ($S_x$=1), the phase current does not pass through the shunt resistor and its magnitude cannot be calculated. Therefore, the current vector can be reconstructed at $V_0$ ($S_AS_BS_C$ = 000), but not at $V_7$ ($S_AS_BS_C$ = 111) [7]. In the carrier based PWM, $V_0$ is placed at the peak and $V_7$ is placed at the valley of the carrier signal. Therefore, when the voltage signal is injected at the carrier frequency in the TSSI, $\Delta i_{dh}^{\hat{r}}$ and $\Delta i_{qh}^{\hat{r}}$ cannot be extracted because $i_{d1}^{\hat{r}}$ and $i_{q1}^{\hat{r}}$ cannot be sampled. Therefore, in the TSSI, the maximum injection frequency is limited to half of the carrier frequency to calculate the rotor angle from Equ. (6).

### *C. Switching Leg According to the Injection Axis*

Fig. 4 shows the voltage vector plane and the modified voltage vectors by the injected voltage signal. Here, the original voltage vector for the current control is located in sector 2. In the $d$-axis injection, the modified voltage vectors are in sectors 1 and 3. In the $q$-axis injection, the modified voltage vectors are in sector 2 and 4. If these modified voltage vectors are modulated with the continuous PWM, all of the legs have two switching events in one sampling period even in the voltage signal injection. This means that the switching loss difference between the $d$-axis and $q$-axis injections is negligibly small.

However, if the modified voltage vector is modulated with the 120° OFF DPWM, the non-switching leg which does not have a switching event for one sampling period is altered in every sampling period. Fig. 5 shows the voltage reference signals and the switching functions according to the injection axis. When a positive voltage is injected, the voltage vector is in sector 1 and leg C has no switching event as shown in Fig. 5 (a). When a negative voltage is injected, the voltage vector is in sector 4 and leg A has no switching. For two carrier periods,

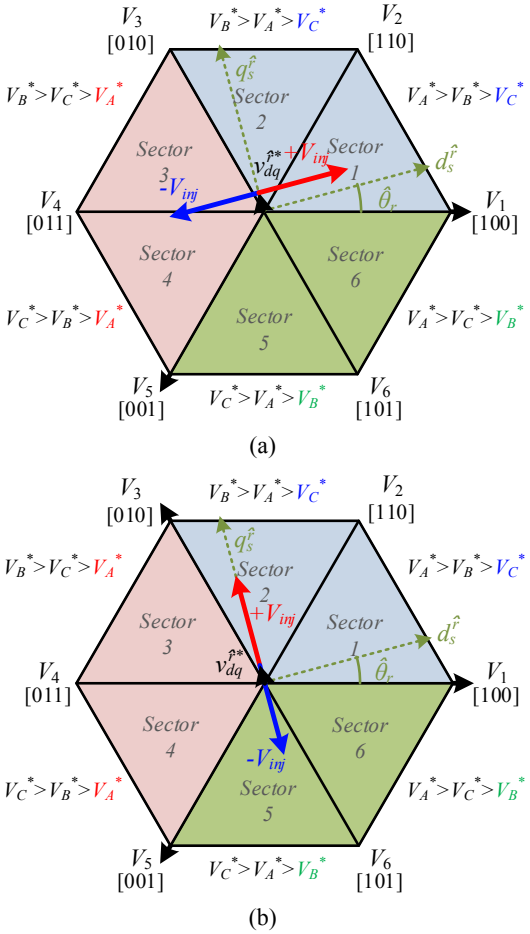


Fig. 4. Modified voltage vectors in voltage signal injection at (a) $d$-axis and (b) $q$-axis.

each leg A and C has two switching events, but leg B has four switching events as shown in Fig. 5(a). When a positive voltage is injected into the $d$-axis, the voltage vector is in sector 2 and leg C has no switching event as shown in Fig. 5(b). When a negative voltage is injected into $q$-axis, the voltage vector is in sector 5 and leg B has no switching. For the two carrier periods, each leg B and C has two switching events, but leg A has four switching events as shown in Fig. 5(b). This means that the switching loss varies with the injection axis.

## IV. Losses According to the Injection Axis

For a more detailed analysis of the switching loss, the switching loss according to the injection axis in the TSSI is analyzed from the mathematical model in [23], [24]. In addition, the conduction losses, copper losses, and iron losses are analyzed in this chapter.

### *A. Switching Loss*

The dissipated energies of the active switch and diode during a switching event depend on the magnitudes of the voltage applied to the device and the current passing through it. The dissipated energies in the active switch and diode

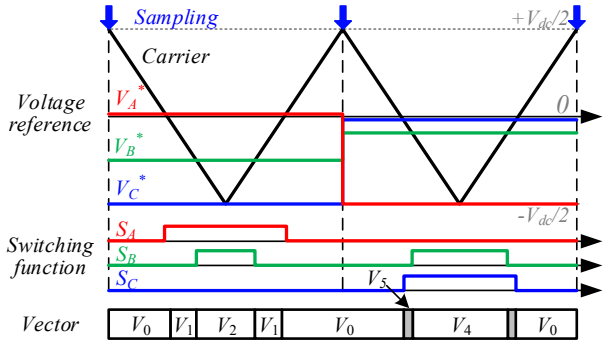


(a)

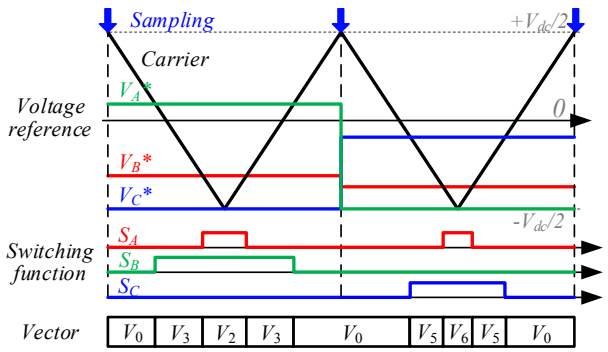


(b)

Fig. 5. Voltage references and switching function of Fig. 4 in 120° OFF DPWM; (a) *d*-axis injection (b) *q*-axis injection.

($w_{active}$, $w_{diode}$) per switching event can be expressed as:

$$w_{active}(\theta) = E_T i_s(\theta),\ w_{diode}(\theta) = E_D i_s(\theta), \quad (7)$$

where $E_{Tx}$ and $E_{Dx}$ are the dissipated energy per ampere of the active switch and diode during on and off switching events. Here, the subscript '$_x$' can be '$_U$' for the upper switch or '$_L$' for the lower switch in each leg. When the DC link voltage is fixed, the dissipated energies are linearly proportional to $i_s$.

The switching loss is a product of the dissipated energy and the switching frequency. In order to calculate the average switching loss, a fundamental period of the phase current is considered. In the continuous PWM, leg A has a switching at the carrier frequency for a fundamental period. The average switching losses of the upper switch ($P_{sw,TU}$) and the upper diode ($P_{sw,DU}$) can be derived as:

$$P_{sw,TU} = E_{TU} I_m \frac{f_{carry}}{\pi},\ P_{sw,DU} = E_{DU} I_m \frac{f_{carry}}{\pi}, \quad (8)$$

where $f_{carrier}$ is the carrier frequency, and $I_m$ is the magnitude of the phase current. If $E_T$=$E_{TU}$=$E_{TL}$ and $E_D$=$E_{DU}$=$E_{DL}$, the total sum of the average switching loss in one leg is:

$$P_{sw,leg} = \frac{2(E_T + E_D) f_{carry} I_{mag}}{\pi}. \quad (9)$$

The average switching loss of a three leg inverter ($P_{sw,total}$) is three times that of $P_{sw,leg}$. It only depends on $f_{carrier}$ and $I_{mag}$ [23].

In the 120° OFF DPWM, when the voltage reference vector is from -180º to -120º and from 120º to 180º, leg A has no switching as shown in Fig. 6. The average switching losses at

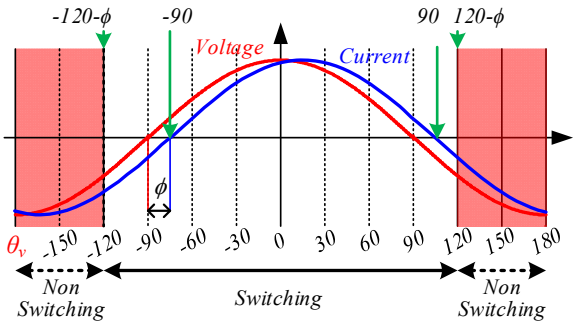


Fig. 6. Phase voltage and current of leg A when -30°<$\phi$<30°.

TABLE II
AVERAGE SWITCHING LOSS OF INVERTER 120° OFF DPWM ACCORDING TO LOAD ANGLE

| Load angle | $P_{sw,total}$ |
|---|---|
| $-\pi/6 < \phi < \pi/6$ | $\frac{3(E_T + E_D) f_{carry} I_m}{\pi}\left[2 - \frac{\sqrt{3}}{2}\cos\phi\right]$ |
| $\pi/6 < \phi < 5\pi/6$ | $\frac{3(E_T + E_D) f_{carry} I_m}{\pi}\left[1 + \frac{1}{2}\sin\phi\right]$ |
| $5\pi/6 < \phi < 7\pi/6$ | $\frac{3(E_T + E_D) f_{carry} I_m}{\pi}\left[2 + \frac{\sqrt{3}}{2}\cos\phi\right]$ |
| $7\pi/6 < \phi < 11\pi/6$ | $\frac{3(E_T + E_D) f_{carry} I_m}{\pi}\left[1 - \frac{1}{2}\sin\phi\right]$ |

the upper switch and the upper diode can be derived as:

$$P_{sw,TU} = E_{TU} I_m \frac{f_{carry}}{\pi}, \quad (10)$$

$$P_{sw,DU} = E_{DU} I_m \frac{f_{carry}}{2\pi}\left(2 - \sqrt{3}\cos\phi\right), \quad (11)$$

where the load angle ($\phi$) is the difference between the angle of the voltage vector ($\theta_v$) and the angle of the current vector ($\theta_i$). If $E_T$=$E_{TU}$=$E_{TL}$ and $E_D$=$E_{DU}$=$E_{DL}$, the total sum of the average switching losses in one leg is:

$$P_{sw,leg} = \frac{(E_T + E_D) f_{carry} I_{mag}}{\pi}\left[2 - \frac{\sqrt{3}}{2}\cos\phi\right], \quad (12)$$

where $-30^\circ < \phi < 30^\circ$. $P_{sw,leg}$ in other angles is calculated in the same manner. The average switching loss of a three leg inverter in the 120° OFF DPWM are summarized in Table II [25]. When the load angle is 0º or 180º, $P_{sw,total}$ has its minimum value. When it is 90º or -90º, $P_{sw,total}$ has its maximum value. The maximum value of $P_{sw,total}$ is 32% larger than the minimum value of $P_{sw,total}$ in the 120° OFF DPWM.

### *B. Switching Losses According to the Injection Axis*

Fig. 7 shows the voltage and current vectors when the voltage signal is injected. The angle of the original voltage vector is over 90° since the positive speed and torque conditions are considered. When a positive voltage ($+V_{inj}$) is added, the original voltage vector from the current controller ($v_{dq}^{\hat{r}*}$) is changed to $v_{dq1}^{\hat{r}*}$. When a negative voltage ($-V_{inj}$) is added, it is changed to $v_{dq2}^{\hat{r}*}$. Here, $\theta_{v1}$ and $\theta_{v2}$ are the angles of

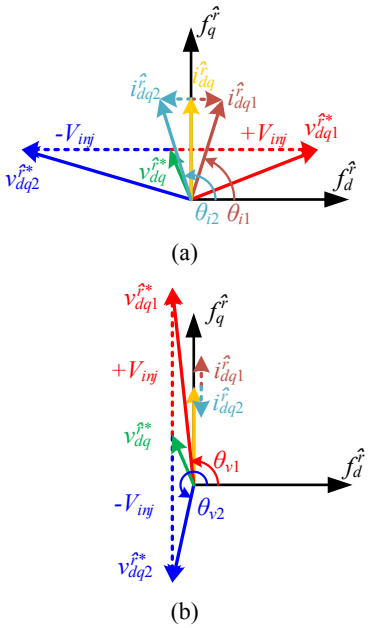


Fig. 7. Modified voltage and current vectors by the voltage signal injection at (a) *d*-axis and (b) *q*-axis.

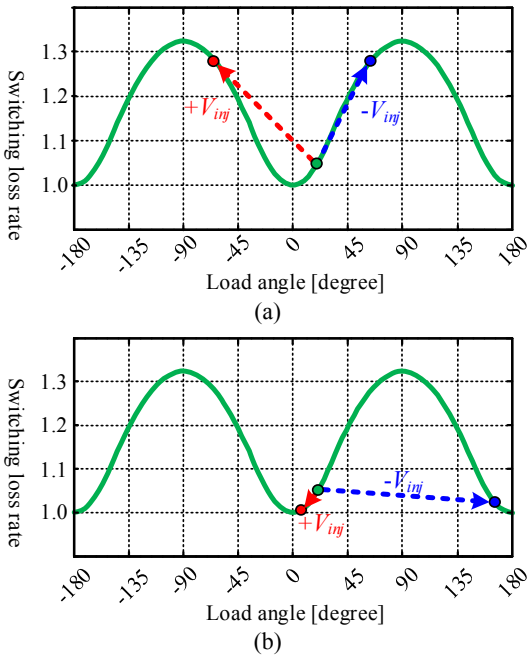


Fig. 8. Relative average switching loss at (a) *d*-axis injection and (b) *q*-axis injection.

$v_{dq1}^{\hat{r}*}$ and $v_{dq2}^{\hat{r}*}$, respectively. In addition, the current vector varies by the voltage injection. $i_{dq1}^{\hat{r}}$ is the current vector after a positive voltage injection, and $i_{dq2}^{\hat{r}}$ is the current vector after a negative voltage injection. Here, $\theta_{i1}$ and $\theta_{i2}$ are the angles of $i_{dq1}^{\hat{r}}$ and $i_{dq2}^{\hat{r}}$, respectively. The average current vector of $i_{dq1}^{\hat{r}}$and $i_{dq2}^{\hat{r}}$ is $i_{dq}^{\hat{r}}$, and it is the same as the current vector without any voltage signal injection.

When the voltage signal is injected at the *d*-axis, the voltage vectors become close to the *d*-axis of the rotor reference frame as shown in Fig. 7(a). The current vector is pulsating in parallel with the *d*-axis. When the voltage signal is injected at the *q*-axis, the voltage vectors become close to the *q*-axis of the rotor reference frame as shown in Fig. 7(b). The current vector is pulsating in parallel with the *q*-axis.

To calculate the switching loss when a voltage signal is injected, the operating points in the positive and negative voltage injections can be considered independently. After calculating the switching loss in each operating point from Equ. (12), the total average switching loss can be calculated as:

$$P_{inj,sw} = P_{sw}^{posi} + P_{sw}^{nega}, \quad (13)$$

where $P_{sw}^{posi}$ and $P_{sw}^{nega}$ are the average switching losses at the positive and negative voltage injections for half of the injection period, respectively. For the calculation of $P_{sw}^{posi}$, $v_{dq1}^{\hat{r}*}$ and $i_{dq2}^{\hat{r}}$ are considered since the current vector is at $i_{dq2}^{\hat{r}}$ when a positive voltage is added. Here, the load angle $\phi_1$ is the difference between $\theta_{v1}$ and $\theta_{i2}$. For the calculation of $P_{sw}^{nega}$, $v_{dq2}^{\hat{r}*}$ and $i_{dq1}^{\hat{r}}$ are considered since the current vector is at $i_{dq1}^{\hat{r}}$ when a negative voltage is added. Here, the load angle $\phi_2$ is the difference between $\theta_{v2}$ and $\theta_{i1}$.

Fig. 8 shows a relative switching loss curve calculated from Table II. Here, the switching loss when the load angle is 0 is considered as the base value. Before the voltage injections, the operating point is slightly higher than the valley point when the machine is at a low speed in the generation mode. When the voltage signal is injected at the *d*-axis, the operating point moves near to each peak point of the switching loss curve as shown in Fig. 8(a). When the voltage signal is injected at the *q*-axis, the operating point moves near to the valley points of the switching loss curve as shown in Fig. 8(b). In other words, the *q*-axis injection case tends to reduce the average switching loss but the *d*-axis injection case tends to increase it in the 120° OFF DPWM.

Fig. 9 shows the relative switching loss according to the rotor speed. Here, the switching loss where its value is minimum in no voltage injection is considered as the base value. It is calculated for a 1kW PMSM with the parameters listed in Table III. Here, the *q*-axis current is 5*A* in all of the speed ranges. The solid line means that both of the modified voltage vectors can be modulated under the limited dc link voltage condition. The doted line means that one modified voltage vector cannot be modulated because of the voltage limitation. At low speeds, the switching loss in the *q*-axis injection case ($P_{sw}^{q-axis}$) is lower than that in the *d*-axis injection case ($P_{sw}^{d-axis}$). At high speeds, $P_{sw}^{q-axis}$ is higher than $P_{sw}^{d-axis}$. When the level of the injection voltage is increased, the speed of the cross point between $P_{sw}^{d-axis}$ and $P_{sw}^{q-axis}$ is increased. This means that when the level of the injection voltage is large, the speed range where $P_{sw}^{q-axis}$ is lower than $P_{sw}^{d-axis}$ is wide.

Therefore, since the saliency based method is commonly

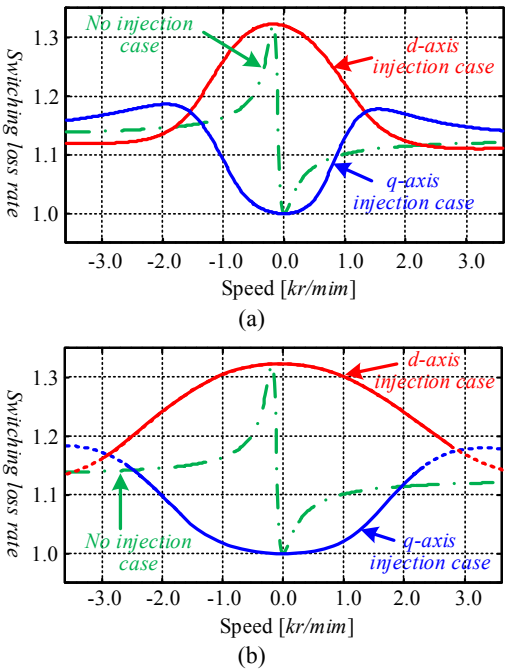


Fig. 9. Relative switching loss according to the rotor speed when (a) $V_{inj}$ =50V and (b) $V_{inj}$=100.

used at low speeds in sensorless control, the $q$-axis injection method in the 120° OFF DPWM has merit. In addition, $P_{sw}^{q-axis}$ is lower than the switching loss in the no injection case ($P_{sw}^{no}$) at low speeds in the generation mode. However, since other losses can be increased by the injected voltage signal, it is hard to say that the $q$-axis injection method in the 120° OFF DPWM is better than the no injection case at low speeds in the generation mode.

### *C. Other Losses According to the Injection Axis*

When current passes through the active switch or diode, there is a voltage drop which causes a conduction loss [24]. The voltage drops of the active switch and diode ($v_T$, $v_D$) can be simply expressed as:

$$v_T = V_T + R_T |i_s|, \quad v_D = V_D + R_D |i_s|, \tag{14}$$

where $V_T$ and $V_D$ are constant voltage drops in the active switch and diode, and $R_T$ and $R_D$ are the on-state slope resistances of the active switch and diode, respectively. The instantaneous conduction loss is a product of the voltage drop and $i_s$. The average conduction losses of the upper active switch ($P_{CON,TU}$) and the upper diode ($P_{CON,DU}$) are derived as:

$$\begin{aligned} P_{CON,TU} &= \frac{1}{2\pi} \int_{i_s>0} v_T \cdot i_s \cdot \xi \, d\theta, \\ P_{CON,DU} &= \frac{1}{2\pi} \int_{i_s>0} v_D \cdot i_s \cdot (1-\xi) d\theta, \end{aligned} \tag{15}$$

where $\xi$ is the on duty of the upper switch. This on duty depends on the PWM method and the load angle.

In sinusoidal wave PWM [23], the sum of the average conduction losses for the upper active switch and the diode is:

TABLE III
PARAMETERS OF MACHINE AND SYSTEM

| Quantity | Value [*Unit*] |
|---|---|
| Rated power | 1 *kW* |
| Number of pole | 6 |
| Rated current | 10 *A* |
| *d*-axis inductance | 8.8 *mH* |
| *q*-axis inductance | 12.9 *mH* |
| Phase resistance | 1.09 *Ω* |
| Rated speed | 3600 *r/min* |
| Shunt resistance | 0.04 *Ω* |

$$\begin{aligned} P_{con,U} &= \frac{I_m}{2\pi}(V_T + V_D) + \frac{I_m}{8}(V_T - V_D) MI \cos\phi \\ &+ \frac{I_m^2}{2}(R_T + R_D) + \frac{I_m^2}{3\pi}(R_T - R_D) MI \cos\phi, \end{aligned} \tag{16}$$

where $MI$ is the modulation index of the voltage reference. If $V_T \approx V_D$ and $R_T \approx R_D$, the second and fourth terms of Equ. (16) are negligibly smaller than the first and third terms of Equ. (16). Since the total conduction loss of the three leg inverter is six times as much as $P_{con,U}$, the simplified total conduction loss is:

$$P_{con} = 6 \times \left[ \frac{I_m}{2\pi}(V_T + V_D) + \frac{I_m^2}{2}(R_T + R_D) \right]. \tag{17}$$

The sum of the average conduction losses for the upper active switch and the diode in the continuous PWM and the 120º OFF DPWM is a function of the on duty and $MI$. However, when $V_T \approx V_D$ and $R_T \approx R_D$, the simplified total conduction losses of the three leg inverter in the continuous PWM and the 120º OFF DPWM are same as those in Equ. (17). This simplified total conduction loss depends on the magnitude of the phase current. but it is independent from the load angle. Even though the rms value of the phase current can be increased because of the voltage injection, the enlargement of the rms value is small at a high injection frequency. This means that the conduction losses of the $d$-axis and $q$-axis injection cases are almost the same.

The machine losses are classified into copper loss and iron loss. The copper loss is a product of the phase resistance ($R_s$) and the square of $I_m$. Therefore, the total copper loss in a three phase machine is:

$$P_{copper} = 3 \times (I_m^2 \cdot R_s). \tag{18}$$

Similar to the conduction loss, the rms value of the phase current is increased, but the increase of the copper loss is small and negligible. In addition, the copper losses of the $d$-axis and $q$-axis injections are almost the same.

The iron loss is the sum of the hysteresis loss and the eddy current loss. The hysteresis loss is proportional to the frequency and level of the rotating flux. In addition, the eddy current loss is proportional to the square of the frequency and level of the rotating flux. Therefore, the iron loss in high frequency injection is larger than that in low frequency

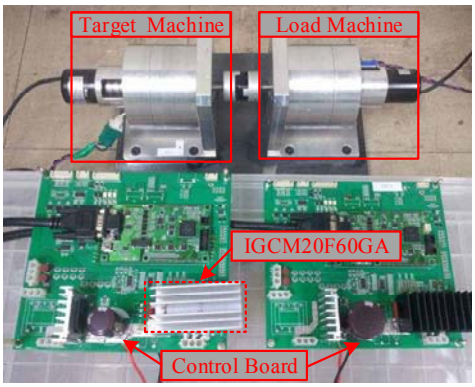


Fig. 10. Experimental setup with 1kW IPMSM.

injection [23]. In [24], the machine losses due to the injection voltage have been studied with computer simulations. The iron loss of the *d*-axis injection case is larger than that in the *q*-axis injection case when $L_q$ is larger than $L_d$. The reason is that the flux level of the *d*-axis injection case is larger than that of the *q*-axis injection case when the same levels of voltage are injected in both cases.

## V. Simulation and Experimental Results

For the simulations and experiments, an 1kw PMSM drive system with the TSSI and the IGBT power module, IGCM20F60GA, were used as shown in Fig. 10. The detailed system parameters are listed in Table III. Since the carrier frequency was set to 30 *kHz*, the average switching frequency was 20 *kHz* with the 120° OFF DPWM. A square wave voltage at 15 *kHz* was added to the output of the current controller and the current signals were sampled at 30 *kHz*. Here, the magnitude of the *q*-axis current in Equ. (3) was controlled to be same as the magnitude of the *d*-axis current in Equ. (4) for the same performance in angle estimation. Therefore, the level of the injection voltage is 100*V* in the *d*-axis and *q*-axis injections. The magnitude of the *d*-axis current ripples was 0.19*A* in the *d*-axis injection case, and that of the *q*-axis current ripples was 0.13*A* in the *q*-axis injection case.

Fig. 11 shows the modulated pole voltages when square wave voltages were injected in the *d*-axis and *q*-axis of the rotor reference frame. A small *d*-axis current was applied to lock the rotor when the rotor angle was 15°. When the voltage signal was injected at the *d*-axis, the *B* phase leg has four switching events for one injection period, which is the same as the two sampling periods. However, when the voltage signal was injected at the *q*-axis, the *A* phase leg has four switching events for one sampling period.

Fig. 12 shows the performances of the angle estimations in the *d*-axis and *q*-axis injection cases. To calculate the angle estimation error, the *q*-axis current of Equ. (3) was used in the *d*-axis injection case, and the *d*-axis current of Equ. (4) was used in the *q*-axis injection case. When the rotating speed of the PMSM was 36r/min, the output torque was controlled with

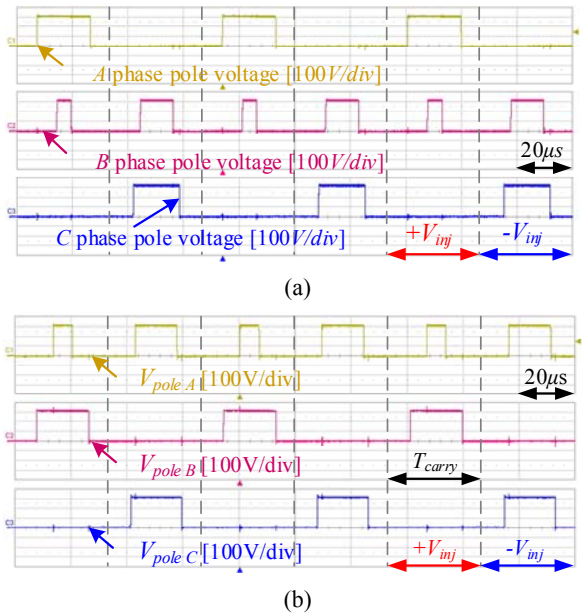


Fig. 11. Modulated pole voltage when the voltage signal is injected in (a) *d*-axis and (b) *q*-axis.

the sensorless method. 70% of the rated torque was commanded and removed. Here, the slop of the torque command was limited to 50 *p.u./s* to obtain the voltage margin for the voltage signal injection. The rotor angle was estimated without failure in the transient conditions. The maximum angle errors were 30° in the *d*-axis injection case and 32° in the *q*-axis injection case. There are no distinct difference between the *d*-axis and *q*-axis injection cases in terms of the performance of the angle estimation.

The inverter and machine losses are calculated with computer simulations. Here, PLECS 3.5 was used as a computer simulator. The characteristics of the IGCM20F60GA were applied from its datasheet. Since an iron loss model of the PMSM is not applied, only the conduction loss, switching loss, and copper loss are considered in this computer simulation. Fig. 13 and Fig. 14 show these losses when the *q*-axis currents are 1*A*, and 10*A*, respectively. To inject a voltage signal at 15 *kHz*, the carrier frequency was set as 15 *kHz* in the continuous PWM and as 30 *kHz* in the 120º OFF DPWM. Therefore, the switching frequency was 15 *kHz* in the continuous PWM and the average switching frequency was 20 *kHz* in the 120º OFF DPWM. Therefore, the switching loss at no injection in the 120º OFF DPWM is larger than that in the continuous PWM in this paper.

As shown in Fig. 13(a), the switching losses of the *d*-axis and *q*-axis injection cases are slightly larger than those of the no injection case. The reason is that the voltage injection increases the rms value of the phase current. As shown in Fig. 14(a) and Fig. 15(a), the switching losses of the *d*-axis injection case, the *q*-axis injection case, and the no injection case are almost the same. The reason is that the current ripple due to the injection voltage is small and negligible when the load current

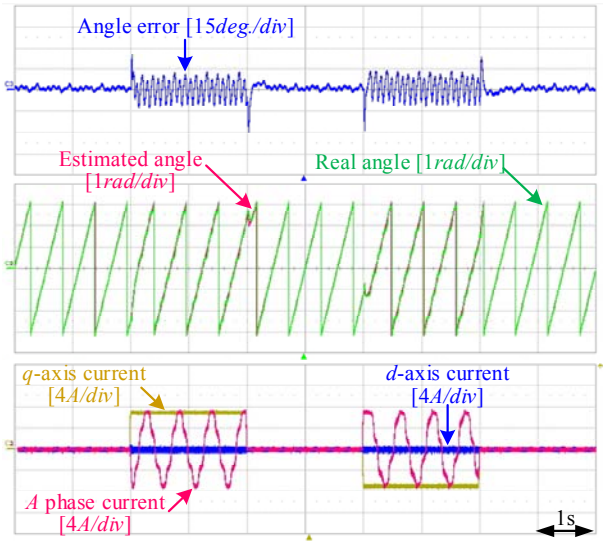


(a)

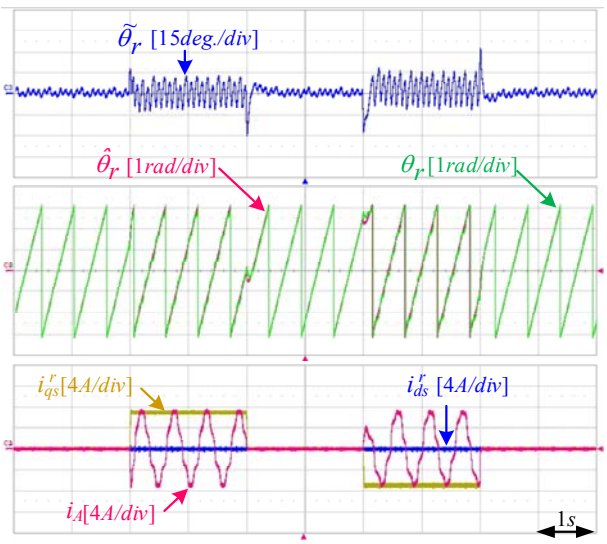


(b)

Fig. 12. Angle estimation error, estimated rotor angle, real rotor angle, and *d*- and *q*-axis currents in (a) the *d*-axis injection case and (b) the *q*-axis injection case.

is relatively large in the continuous PWM.

As shown in Fig. 13(b), Fig. 14(b), and Fig. 15(b), the switching loss of the *d*-axis injection case is larger than that of the *q*-axis injection case in the 120° OFF DPWM. Under some conditions, the switching loss of the *q*-axis injection case is even smaller than that of the no injection case. The reason is that the operating points move when the switching loss is small due ot the injected voltage signal in the *q*-axis injection case. The switching losses of the *d*-axis injection case are 28~33% larger than those of the *q*-axis injection case. These values are similar to the analysis results in the section III.

As shown in Fig. 13, Fig. 14, and Fig. 15, the conduction losses and copper losses depend on the rms value of the phase current regardless of the injection cases. When the *q*-axis current is 1*A*, the conduction loss and copper loss of the *d*-axis

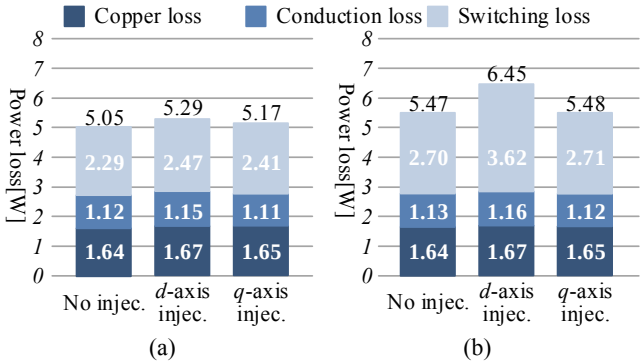


Fig. 13. Power losses from computer simulations when the *q*-axis load current is 1*A* at 36*r/min* with (a) Continuous PWM ($f_{carry}$=15*kHz*) and (b) 120˚ OFF DPWM ($f_{carry}$=30*kHz*).

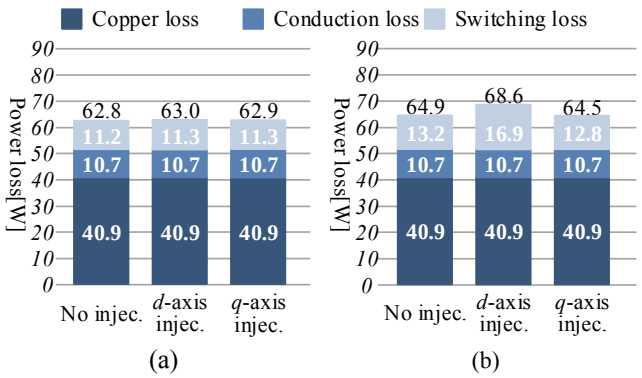


Fig. 14. Power losses from computer simulations when the *q*-axis load current is 5*A* at 36*r/min* with (a) Continuous PWM ($f_{carry}$=15*kHz*) and (b) 120˚ OFF DPWM ($f_{carry}$=30*kHz*).

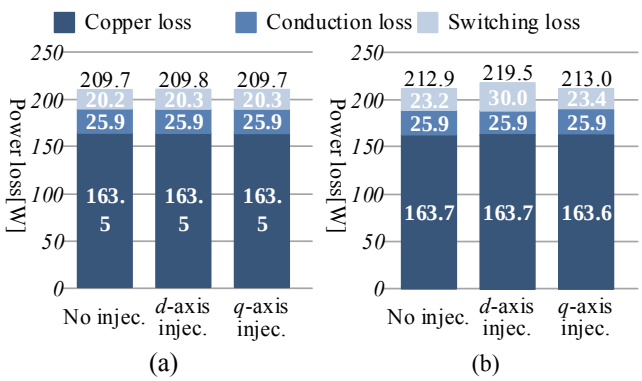


Fig. 15. Power losses from computer simulations when the *q*-axis load current is 10*A* at 36*r/min* with (a) Continuous PWM ($f_{carry}$=15*kHz*) and (b) 120˚ OFF DPWM ($f_{carry}$=30*kHz*).

or *q*-axis injection cases are slightly larger than those of the no injection case. When the *q*-axis currents are 5*A* and 10*A*, the conduction losses and copper losses of the three injection cases are almost the same.

In the experiments, the power input of the inverter was measured by a power meter, PPA5530. By subtracting the output power of the machine from the input power, the total loss was calculated. Fig. 16, Fig. 17, and Fig. 18 show the total losses in the no injection case and in the *d*-axis and *q*-axis injection cases when the *q*-axis currents are 1*A*, 5*A*, and 10*A*,

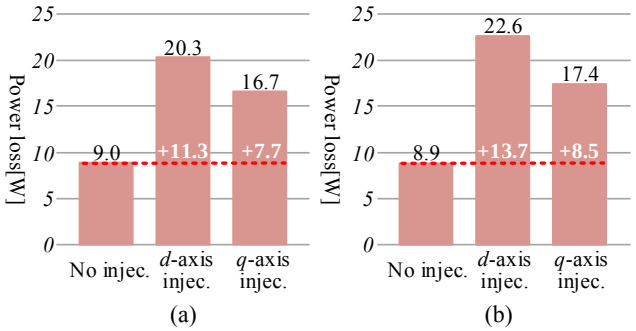


Fig. 16. Total losses from the experimental results when the $q$-axis load current is 1$A$ at 36$r/min$ with (a) Continuous PWM ($f_{carry}$=15$kHz$) and (b) 120˚ OFF DPWM ($f_{carry}$=30$kHz$).

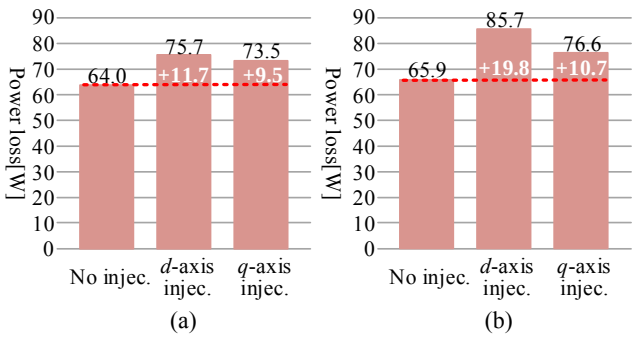


Fig. 17. Total losses from the experimental results when the $q$-axis load current is 5$A$ at 36$r/min$ with (a) Continuous PWM ($f_{carry}$=15$kHz$) and (b) 120˚ OFF DPWM ($f_{carry}$=30$kHz$).

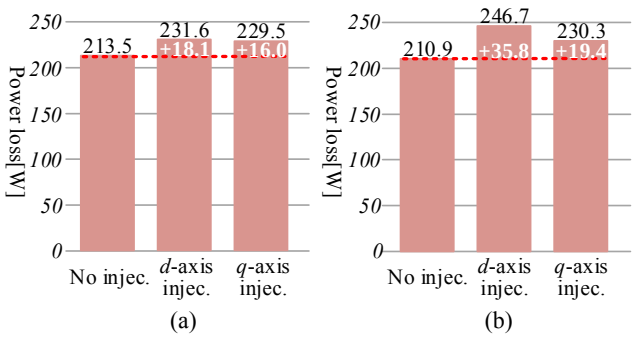


Fig. 18. Total losses from the experimental results when the $q$-axis load current is 10$A$ at 36$r/min$ with (a) Continuous PWM ($f_{carry}$=15$kHz$) and (b) 120˚ OFF DPWM ($f_{carry}$=30$kHz$).

respectively. The total loss includes the iron loss which is not considered in the simulations. According to the simulation results, the sum of the switching loss, the conduction loss and the copper loss of no injection case is similar to that of the $d$-axis or $q$-axis injection cases in the continuous PWM. Therefore, the difference between the total loss in the no injection case and that of the $d$-axis or $q$-axis injection case in the continuous PWM is mostly the incensement of the iron loss by the voltage signal injection. As shown in Fig. 16(a), Fig. 17(a), and Fig. 18(a), the incensements of the iron loss were from 11.3W to 18.1W in the $d$-axis injection case and from 7.7W to 16.0W in the $q$-axis injection case. Since $L_q$ is larger than $L_d$ in this machine, the flux ripples in the $d$-axis injection case are larger than those in the $q$-axis injection case. Therefore, the iron loss in the $d$-axis injection case is larger than that in the $q$-axis injection case.

The difference between the total loss of the no injection case and that of the $d$-axis or $q$-axis injection case in the 120º OFF DPWM is relatively large when compared to that in the continuous PWM. As shown in Fig. 16(b), Fig. 17(b), and Fig. 18(b), the incensements of the iron loss were from 13.7W to 35.8W in the $d$-axis injection case and from 8.5W to 19.4W in the $q$-axis injection case. Since the switching loss of the $d$-axis injection case is larger than that of the $q$-axis injection case in the 120º OFF DPWM, the difference of the total loss of the $d$-axis and $q$-axis injection cases is increased. Therefore, when the voltage signal is injected at a high frequency in the 120º OFF DPWM, the $q$-axis injection case can reduce the total power loss when compared to the $d$-axis injection case.

## VI. CONCLUSIONS

This paper considered the high frequency injection method in the TSSI for sensorless motor control. In addition, it analyzed the switching losses according to the injection axis at the carrier frequency injection in detail. When both the phase current reconstruction and the sensorless methods use a voltage signal simultaneously, an interaction problem can be incurred. To avoid this interaction problem, a signal injection based sensorless method with the 120º OFF DPWM in the TSSI is considered in this paper. In the 120º OFF DPWM, the switching loss is altered according to the direction of the voltage signal injection since one leg does not have a switching event for one sampling period. In the $d$-axis injection case, the load angles between the modified voltage vectors and the current vector are close to 90º or -90º. In the $q$-axis injection case, the load angles are close to 0º or 180º. Therefore, the switching loss of the $d$-axis injection case can be up to 32% larger than that of the $q$-axis injection case. Since the current ripple by the injection voltage is small, the conduction loss and copper loss do not depend a lot on the injection axis. However, because of the flux ripple, the iron loss of the $d$-axis injection case is larger than that of the $q$-axis injection case. Therefore, the $q$-axis injection case with the 120º OFF DPWM in the TSSI can significantly reduce the total power loss in the low speed range. This analysis was verified by simulation and the experimental results.

## ACKNOWLEDGMENT

This work was supported by Brain Korea 21 Plus Creative Research Engineer Development IT and Seoul National University Electric Power Research Institute.

## REFERENCES

[1] A. Dianov, N.-S. Kim, and Y.-K. Kim, “Foture drives of home appliances: Elimination of the electrolytic DC-link capacitor in electrical drives for home appliances,” *IEEE*

*Trans. Ind. Elec. Magazine*, Vol. 9, No. 3, pp. 10-18, Sep. 2015.

[2] W.-C. Lee, D.-S. Hyun, and T.-K. Lee, "A novel control method for three-phase PWM rectifiers using a single current sensor," *IEEE Trans. Power Electron*., Vol. 15, No. 5, pp. 861-870, Sep. 2000.

[3] H. Kim and T. Jahns, "Phase current reconstruction for AC Motor drives using a DC link single current sensor and measurement voltage vectors," *IEEE Trans. Power Electron*., Vol. 21, No. 5, pp. 1413-1419, Sep. 2006.

[4] J.-I. Ha, "Voltage injection method for three-phase current reconstruction in PWM inverters using a single sensor," *IEEE Trans. Power Electron*., Vol. 24, No. 3, pp. 767-775, Mar. 2009.

[5] J.-I. Ha, "Current prediction in vector-controlled PWM inverters using single DC-Link current sensor," *IEEE Trans. Ind. Elec*., Vol. 57, No. 2, pp. 714-726, Feb. 2010.

[6] H. Shin and J.-I. Ha, "Phase current reconstructions from DC-link currents in Three-Phase Three-Level PWM inverters," *IEEE Trans. Power Electron*., Vol. 29, No. 2, pp. 582-593, Feb. 2014.

[7] B.-G. Cho, J.-I. Ha, and S.-K. Sul, "Analysis of the phase current measurement boundary of three shunt sensing PWM inverters and an expansion method." *Journal of Power Electronics*, Vol. 13, No. 2, pp. 326-335, Mar. 2013.

[8] N. Matusi, "Sensorless PM brushless DC motor drives," *IEEE Trans. Ind. Electron*., Vol. 43, No. 2, pp. 300-308, Apr. 1996.

[9] S. Morimoto, K. Kawamoto, M. Sanada, and Y. Takeda, "Sensorless control strategy for salient-pole PMSM based on extended EMF in rotating reference frame," *IEEE Trans. Ind. Appl.*, Vol. 38, No. 4, pp. 1054-1061, Jul./Aug. 2002.

[10] K.-G. Lee, J.-S. Lee, and K.-B. Lee, "Wide-range sensorless control for SPMSM using an improved full-order flux observer." *Journal of Power Electronics*, Vol. 15, No. 3, pp. 721-729, May 2015.

[11] K.-W. Lee, "Compensation of periodic magnetic saturation effects for the high-speed sensorless control of PMSM driven by inverter output power control-based PFC strategy." *Journal of Power Electronics*, Vol. 15, No. 5, pp. 1264-1273, Sep. 2015.

[12] J.-W. Kim and J.-I. Ha, "Accuracy enhancement of parameter estimation and sensorless algorithms based on current shaping," *Journal of Power Electronics*, Vol. 16, No. 1, pp. 1-8, Jan. 2016.

[13] J. -I. Ha, and S. -K. Sul, "Sensorless field-orientation control of an induction machine by high-frequency signal injection," *IEEE Trans. Ind. Appl*., Vol. 35, No. 1, pp. 45-51, Jan./Feb. 1999.

[14] Y. D. Yoon, S. K. Sul, S. Morimoto, and K. Ide, "High-bandwidth sensorless algorithm for AC machines based on square-wave-type voltage injection," *IEEE Trans. Ind. Appl.*, Vol. 47, No. 3, 1361-1370, May/Jun. 2011.

[15] S. Kim, J. I. Ha, and S. K. Sul, "PWM switching frequency signal injection sensorless method in IPMSM," *IEEE Trans. Ind. Appl.*, Vol. 48, No. 5, pp. 1576-1587, Sep./Oct. 2012.

[16] Z. Chen, X. Deng, K. Huang, W. Zhen, and L. Wang, "Sensorless control of wound rotor synchronous machines based on high frequency signal injection into the stator windings," *Journal of Power Electronics*, Vol. 13, No. 4, pp. 669-678, Jul. 2013.

[17] S. Jung and J.-I.Ha, "Analog filtering method for sensorless AC machine control with carrier frequency signal injection," *IEEE Trans. Ind. Electron*., Vol. 62, No. 9, pp. 5348-5336, Sep. 2015.

[18] S.-C. Y, and R. D. Lorenz, "Comparison of resistance -based and inductance-based self-sensing controls for surface permanent-magnet machines using high-frequency signal injection," *IEEE Trans. Ind. Appl*., Vol. 48, No. 3, pp. 977-986, May/Jun. 2012.

[19] N. Limsuwan, T. Kato, C. -Y. Yu, J. Tamura, D. D. Reigosa, K. Ahatsu, and R. D. Lorenz, "Secondary resistive losses with high-frequency injection-based self-sensing in IPM machines," *IEEE Trans. Ind. Appl*., Vol. 49, No. 4, pp. 1499-1507 Jul./Aug. 2013.

[20] S. Jung and J.-I. Ha "Carrier signal injection method in three shunt sensing inverter for sensorless AC machine drive," in *proc. Energy Conversion Congress and Exposition(ECCE)* 2014, pp. 4154-4161, 2014.

[21] S.-C. Yang, "Saliency-based position estimation of permanent - magnet synchronous machines using square - wave voltage injection with a single current sensor," *IEEE Trans. Ind. Appl*., Vol. 51, No. 2, pp. 1561-1571, Mar./Apr. 2015.

[22] M. Mamo, K. Ide, M. Sawamura, and J. Oyama, " Novel rotor position extraction based on carrier frequency component method (CFCM) using two reference frames for IPM drives," *IEEE Trans. Ind. Electron.*, Vol. 52, No. 2, pp. 508-514, Apr. 2005.

[23] J. W. Kolar, H. Ertl, and F. C. Zach, "Influence of the modulation method on the conduction and switching losses of a PWM converter system," *IEEE Trans. Ind. Appl*., Vol. 27, No. 6, pp. 1063-1075, Nov./Dec. 1991.

[24] D.-W. Chung, and S. -K. Sul, "Minimum-loss strategy for three phase PWM rectifier," *IEEE Trans. Ind. Electron*., Vol. 46, No. 3, pp. 517-526, Jun. 1999.

[25] Y. Wu, M. A. Shafi, A. M. Knight, and R. A. McMahon, "Comparison of the effects of continuous and discontinuous PWM schemes on power losses of voltage sourced inverters for induction motor drives," *IEEE Trans. Power Electron*., Vol. 26, No. 1, pp. 182-191, Jan. 2011.

**Sungho Jung** was born in Busan, Korea, in 1984. He received his B.S. degree in Electronic and Electrical Engineering from Pusan National University, Busan, Korea, in 2010; and his M.S. and Ph.D. degrees in Electrical and Computer Engineering from Seoul National University, Seoul, Korea, in 2012 and 2016; where he is presently working as a Postdoctoral Researcher. His current research interests include electric machine drives and power conversion systems.

**Jung-Ik Ha** was born in Korea, in 1971. He received his B.S., M.S., and Ph.D. degrees in Electrical Engineering from Seoul National University, Seoul, Korea, in 1995, 1997, and 2001, respectively. From 2001 to 2002, he was a Researcher at the Yaskawa Electric Corporation, Kitakyushu, Japan. From 2003 to 2008, he was a Senior and Principal Engineer at Samsung Electronics Co., Korea. From 2009 to 2010, he was the Chief Technology Officer at LS Mecapion Co., Korea. Since 2010, he has been with the Department of Electrical and Computer Engineering, Seoul National University, where he is presently working as an Associate Professor. His current research interests include the circuits and control for high efficiency and integrated electric energy conversions in various industrial fields.